International Journal of Energy Research

INTERNATIONAL JOURNAL OF ENERGY RESEARCH
Int. J. Energy Res. 2015; **39**:1890–1908
Published online 27 August 2015 in Wiley Online Library (wileyonlinelibrary.com). DOI: 10.1002/er.3374

Effects of rate law formulation on predicting CO_2 sequestration in sandstone formations

Guanru Zhang[1,2], Peng Lu[2,3], Yilun Zhang[2], Xiaomei Wei[1,*,†] and Chen Zhu[2,*,†]

[1]College of Water Resources and Architectural Engineering, Northwest A&F University, Yangling 712100, China
[2]Department of Geological Sciences, Indiana University, Bloomington, IN 47408, USA
[3]EXPEC Advanced Research Center, Saudi Aramco, Dhahran 31311, Saudi Arabia

SUMMARY

Injection of CO_2 into confined geological formations, given their massive carbon storage capacity and widespread geographic distribution, represents one of the most promising options for CO_2 sequestration. Reactive transport models have been constructed to understand the process of carbon storage and predict the fate of injected CO_2. Model results, however, differ dramatically because of the large uncertainties attributed to reaction kinetics. The root of this problem is partly related to the one of the biggest challenges in modern geochemistry: The persistent two to five orders of magnitude discrepancy between laboratory-measured and field-derived feldspar dissolution rates. Recently, advances in reaction kinetics research suggest that the slow precipitation of secondary minerals produces negative feedback in the dissolution–precipitation loop, which reduces the overall feldspar dissolution rates by orders of magnitude. In this study, we focused on how the coupling between feldspar dissolution and secondary mineral precipitation, as well as mineral carbonation, is affected by rate law uncertainties. Reactive transport models with four different rate law scenarios were used for CO_2 sequestration in a sandstone formation resembling the Mt. Simon saline reservoir in the Midwest, USA. The results indicate that (1) long-term mineral trapping is more sensitive to rate laws for feldspar dissolution than to rate laws for carbonate mineral precipitation and (2) negligence of the sigmoidal shape of rate – ΔG_r relationships and the mitigating effects of secondary mineral precipitation can overestimate both the extent of feldspar dissolution during CO_2 injection and in turn mineral trapping. Copyright © 2015 John Wiley & Sons, Ltd.

KEY WORDS

CO_2 storage; CO_2–water–rock interactions; reactive transport modeling; rate laws; mineral trapping

Correspondence

*Xiaomei Wei, College of Water Resources and Architectural Engineering, Northwest A&F University, Yangling 712100, China and Chen Zhu, Department of Geological Sciences, Indiana University, Bloomington, IN 47408, USA.
†E-mail: weixiaomei@nwsuaf.edu.cn; chenzhu@indiana.edu

Received 9 April 2015; Revised 11 June 2015; Accepted 25 June 2015

1. INTRODUCTION

Underground storage of carbon dioxide is a viable option for the mitigation of greenhouse gasses because of the reduction of CO_2 to the atmosphere [1–4]. CO_2 is trapped in underground reservoirs by four storage mechanisms [5,6]: (1) Supercritical CO_2 phase rises because of its lower density and eventually is accumulated beneath a lower permeability cap rock (structural trapping); (2) a part of CO_2 reacts with brine to form aqueous species such as $CO_{2,aq}$, $HCO^-_{3,aq}$, or $CO^{2-}_{3,aq}$ (solubility trapping); (3) some CO_2 is trapped by capillary force, remaining in porous media as an immobile form (residual trapping); and (4) some CO_2 reacts with formation minerals to form carbonate minerals (mineral trapping). Mineral trapping is considered the safest mechanism in the long-term storage of CO_2 [7].

Previous reactive transport models (RTM) have provided significant insights towards understanding the process of carbon storage and predicting the fate of injected CO_2 [8–11]. Almost all previous modelers, however, acknowledge that reaction kinetics remain the most uncertain parameters. Not surprisingly, the calculated results from various authors differ dramatically. Some authors predict a significant reduction of porosity in shale [12] while others predict only a slight initial reduction or an increase of porosity for the Sleipner project in Norway [9,13]. The root of these problems is partly related to the persistent two to five orders of magnitude discrepancy between laboratory-measured and field-derived feldspar dissolution rates [14–16].

We focus on the mineral feldspars because feldspar is the most abundant mineral on the earth's crust, making up more than 51% of the crust's volume. Typically,

sandstones, and shale contain a high percentage of feldspar. For example, the Utsira formation has 10–15% feldspars. Mt. Simon sandstone, a potential target for carbon sequestration in the Midwest of the USA, contains about 20% feldspar [10]. Eau Claire shale, Mt. Simon sandstone's caprock, contains an average of ~20% feldspar. Although feldspar dissolution rates are usually slow (in the order of 10^{-8} to 10^{-12} mol/m^2/s) in the temperature range of geological carbon sequestration [14], the extent of water–feldspar reaction is significant because of the long timescale of CO_2 storage (10,000 years or longer) and the corrosive nature of the acid brine due to CO_2 invasion. Feldspar dissolution can also consume H^+, which promotes the precipitation of carbonate minerals and enhances the safety of CO_2 sequestration.

Advances in reaction kinetics research have narrowed this gap between field and lab rates. The coupling of dissolution of feldspar and secondary mineral precipitation results in negative feedback and slows down further dissolution of feldspar [17–21]. How these reactions are coupled depends on rate laws and surface areas [20]. These results suggest that it is likely that most previous RTM simulations of long-term CO_2 fate have overpredicted the extent of reactions (e.g., feldspar dissolution, clay precipitation, and carbonate mineralization) and have overestimated the acid buffering and mineral trapping capacities, as well as porosity/permeability changes.

A number of experiments near equilibrium have shown that the traditional linear rate law (transition state theory (TST)) deviates from the actual relationship between reaction rate and Gibbs free energy of the reaction [22–24]. Different rate laws have been proposed to resolve this deviation, such as Burch-type, and Alekseyev-type nonlinear rate law for feldspar dissolution [22,23] and Burton–Cabrera–Frank (BCF) rate law for secondary mineral precipitation [25,26].

Studies on the effects of different rate laws on the CO_2 trapping processes in the saline aquifer are scarce. We investigated a sandstone formation resembling the Mt. Simon saline reservoir, which contains abundant feldspar. Four rate law scenarios were constructed for the RTM of CO_2 sequestration in order to explore whether uncertainties of the rate laws have a large effect on CO_2 sequestration, how these effects work, and what role the coupling between feldspar dissolution and secondary mineral precipitation plays in the effect.

2. GEOLOGICAL SETTINGS

The Cambrian Mt. Simon sandstone is a widespread saline reservoir, underlying most of the Illinois Basin, which includes most of Illinois, western Indiana, and western Kentucky at depths close to the surface to over 4600 m [27]. The Mt. Simon sandstone is poorly sorted and consists of fine-grained to very coarse-grained and angular to sub-rounded quartz sand grains. It is also poorly consolidated, even though a small amount of silica cement has been observed in some areas. Shale is present throughout the formation in beds ranging from a few centimeters to approximately 19 m in thickness [28]. Running southeastward from Illinois, Mt. Simon thins. The thickness in Illinois is about 516 m, with maximum thickness of close to 700 m found in cuttings from a test well in Kankakee County, northeastern Illinois. The formation decreases to a thickness of less than 60 m in southeastern Indiana and is absent in southwestern Ontario [29]. The top of Mt. Simon is estimated to be from close to surface in the north to over 4848 m in the south [27]. The porosity of the upper part of Mt. Simon (0–760 m) ranges between 10% and 36%; the middle part (760–2400 m) mostly falls between 0% and 20%; the lower arkose zone (2400–4600 m) has a much lower porosity, less than 5% [30].

Mt. Simon sandstone is overlain by three thick and impermeable shale layers (Eau Claire, Maquoketa, and New Albany), and Eau Claire is the most immediate caprock [31]. Well core samples suggest that the Eau Claire formation is thicker in southwest Indiana, thinning to the northwest. The thickness ranges from ~122 m in northeastern Indiana to more than 305 m in southwestern Indiana [28,32]. The formation in northern Indiana is predominantly sandstone, while siltstone, shale, dolomite, and limestone are more prominent in the southern and eastern parts [28].

One million metric tons of CO_2 is planned to be injected into Mt. Simon sandstone over a period of 3 years, conducted by the Archer Daniels Midland Company (ADM), the Midwest Geological Sequestration Consortium (MGSC), and the Illinois State Geological Survey [33]. The CO_2 is provided by ADM from its ethanol plant in Decatur, Illinois. The project started in 2008 with the injection well drilling, and CO_2 injection was scheduled to take place from 2009 to the end of 2012. The target of the project is to determine the best approach for capturing and storing CO_2 that might contribute to global climate change [34].

3. MODELING APPROACH

3.1. Conceptual model

A CO_2 injection well is assumed to penetrate fully the homogeneous and isotropic sandstone formation of 10-m thickness and at a depth of 2 km. Supercritical CO_2 is injected into the sandstone layer at a rate of 1 kg/s along with the co-injected brine (chemical composition is the same as initial formation water) at a rate of 0.5 kg/s for 100 consecutive years. If implemented on the scale of the Mt. Simon formation with representative thickness of 516 m, this modeled injection rate could be scaled up to millions of tons of CO_2 per year. Brine co-injection with CO_2 is suggested to promote residual trapping and enhances dissolution of the CO_2

[35,36]. This might induce the 'salting out' effect that is considered by the simulator in the succeeding text [37]. After the 100 years co-injection period, the brine is injected alone at a rate of 0.5 kg/s without CO_2 until the end of simulation (10,000 years) to represent approximately the return to the regional groundwater flow post-CO_2 injection.

3.2. Modeling code

The simulations in the present study are conducted with the computer code TOUGHREACT with ECO2N module. TOUGHREACT is a numerical simulation program for chemically reactive non-isothermal, density-dependent flows of multi-phase fluids in porous and fractured media [38]. The code can handle a variety of equilibrium chemical reactions, such as aqueous complexation, gas dissolution/exsolution, and cation exchange. Mineral dissolution/precipitation can be subject to either local equilibrium or kinetic controls. For kinetic mineral reactions, TOUGHREACT uses a rate expression from Lasaga *et al.* [39], and the rate constant is dependent on temperature and a variety of different mechanisms (such as neutral, acid, and base mechanisms). A specific fluid property module ECO2N has been designed for multiphase flow dynamics to simulate geologic sequestration of CO_2 in saline aquifers [40]. ECO2N can simulate the fluid property (e.g., density, viscosity, and enthalpy) in the system H_2O–NaCl–CO_2, considering two fluid phases: a water-rich aqueous phase and a CO_2-rich gas phase.

3.3. Grid design and hydrogeologic parameters

A radially symmetric grid model is set up in this study. The layer thickness is 10 m, and grid block sizes increase logarithmically from the wellbore at the origin to the outer boundary of the model, which is approximately 10,000 m.

A constant pressure of 200 bars (representing a reservoir depth ~2000 m) is assigned to the aquifer initially to ensure the supercritical CO_2 flow along the entire formation. Reservoir pressure is allowed to build up because of CO_2 injection. The aquifer temperature is 75 °C. Minor perturbation to the temperature may occur because of the injection [41], but this perturbation is not considered in the simulations. Hydrological properties of the formation are listed in Table I.

The boundary condition applied to our simulations for solving the reactive transport equations is a Dirichlet boundary condition. This Dirichlet boundary is implemented by assigning a large (infinite) volume to the boundary grid block [42]. Consequently, any influence from the influx becomes negligible when compared with the large volume of the formation brine. The aqueous chemical composition of the boundary element, as well as its thermodynamic conditions, such as temperature and pressure, is therefore kept essentially unchanged from the original formation brine [42]. The sandstone layer is initially saturated with water ($S_w = 1$).

3.4. Mineral and formation water composition

Initial mineral composition is listed in Table II. As the formation water contains small amount of S (Table III), potential secondary sulfates such as anhydrite and alunite are included. Gypsum is excluded, because anhydrite is the thermodynamic stable phase at the formation temperature of 75 °C.

The chemical composition for the formation water (Table III) is taken from Eliasson *et al.* [43]. Prior to simulating reactive transport, a batch kinetic modeling of water–rock interaction is performed with the rate laws and kinetic data in the Base case, to equilibrate approximately the measured aqueous chemical composition and the initial minerals. A nearly steady-state aqueous solution composition is obtained, which is used as the initial brine conditions in the models.

Equilibrium constants for the aqueous species and minerals are obtained from the thermodynamic database of EQ3/6 V7.2b with several revisions, following Xu *et al.* [44]. Local equilibrium is assumed to be attained by all reactions among the aqueous species in our simulations. Only two mineral reactions, calcite and anhydrite, are governed by the local equilibrium because of their fast reaction rates.

3.5. Kinetics of mineral reactions

3.5.1. Rate law

Traditionally, kinetically controlled mineral dissolution and precipitation are described by a general form of rate law [45,39],

$$\frac{r}{S} = \pm k a_{H^+}^{i} (f\Delta G_r) \tag{1}$$

where, r denotes the dissolution/precipitation rate in mol/s/kg H_2O, S is the reactive surface area per kilogram H_2O, k is temperature-dependent rate constant (mol/m^2/s), $a_{H^+}^{i}$ is the activity of H^+, and i is the empirical reaction order accounting for catalysis by H^+ in solution. $f(\Delta G_r)$ is the rate dependence on Gibbs free energy of the reaction ΔG_r, the chemical driving force of the reaction.

Generally, reactive transport modeling simulations used the $f(\Delta G_r)$ based on the TST for elementary reactions [46,47],

$$f(\Delta G_r) = 1 - \exp\left(\frac{\Delta G_r}{RT}\right) \tag{2}$$

A number of experiments near equilibrium, however, have shown that the actual relationship between r and

Int. J. Energy Res. 2015; **39**:1890–1908 © 2015 John Wiley & Sons, Ltd.
DOI: 10.1002/er

Table I. Hydrogeologic parameters for the Mt. Simon sandstone formation.

Parameters	Adopted values	Range	References
Permeability (m^2)	10^{-13}		Liu *et al.* [10]
Porosity	0.15		Liu *et al.* [10]
Thickness (m)	500		Liu *et al.* [10]
Temperature (°C)	75	20–150	Eliasson *et al.* [43]; Hovorka *et al.* [56]; Leeper [57]
Pressure (bar)	200	70–420	Eliasson *et al.* [43]; Hovorka *et al.* [56]
CO_2 injection rate (kg/s)	1 (at 0–100 years)		
Co-injected brine rate (kg/s)	0.5		
Relative permeability			
Liquid [56]:			
$k_{rl}=\sqrt{S^*\left\{1-\left(1-[S^*]^{1/m}\right)^m\right\}^2}$	$S^*=(S_l-S_{lr})/(1-S_{lr})$		
S_{lr}: irreducible water saturation	0.3	0.22–0.46	Krevor *et al.* [59]
m: exponent	0.58		
Gas [60]:			
$k_{rg}=(1-\hat{S})^2\left(1-\hat{S}^2\right)$	$\hat{S}=\frac{(S_l-S_{lr})}{(1-S_{lr}-S_{gr})}$		
S_{gr}: irreducible gas saturation	0.1	Maximum 0.21	Krevor *et al.* [59]
Capillary pressure [56]:			
$P_{cap}=-P_o([S^*]^{-1/m}-1)^{1-m}$	$S^*=(S_l-S_{lr})/(1-S_{lr})$		
S_{lr}: irreducible water saturation	0.3	0.22–0.46	Krevor *et al.* [59]
m: exponent	0.45		
P_o: strength coefficient (kPa)	6.6		Krevor *et al.* [59]

ΔG_r deviates from this so-called linear rate law in Equation (2) [21,23,24]. For feldspar dissolution, for example, different nonlinear rate laws were proposed. Burch *et al.* [23] discovered that feldspar dissolution reactions follow the empirical parallel rate law in the form of

$$r/S = k_1\left[1-\exp\left(-ng^{m1}\right)\right]+k_2[1-\exp(-g)]^{m2} \quad (3)$$

where k_1 and k_2 denote the rate constants in units of mol/m^2/s, $g=|\Delta G_r|/RT$, and n, m_1, and m_2 are empirical parameters fitted from experimental data [15].

Alekseyev *et al.* [22] introduced another nonlinear rate law in the form of

$$f(\Delta G_r)=\left|1-\left(\frac{Q}{K}\right)^p\right|^q \quad (4)$$

where Q is the activity quotient, K is the equilibrium constant, p and q are fitting parameters.

Another source of kinetic uncertainties is that previous reactive transport modeling work generally used the same rate expressions for both dissolution and precipitation, which may lead to large errors. For example, using the TST based rate law along with this assumption leads to high precipitation rates even at low supersaturation [48]. Moreover, the first order dependence on saturation state used for dissolution does not fit with the second order dependence observed for precipitation [26].

Alternatively, BCF theory for crystal growth [25] can be used for secondary mineral precipitation,

$$f(\Delta G_r)=\left(\exp\left(\frac{\Delta G_r}{RT}\right)-1\right)^2 \quad (5)$$

Saldi *et al.* [26] found that this rate law satisfactorily describes the experimental data of magnesite precipitation. BCF-type rate law has successfully simulated secondary mineralization in feldspar hydrolysis experiments [19].

To explore whether uncertainties of the rate laws have a large effect on CO_2 sequestration, how these effects work, and what role the coupling between feldspar dissolution and secondary mineral precipitation plays in the effect, we constructed four scenarios using different rate laws for mineral reactions.

3.5.1.1. Scenario 1: Base case. Transition state theory rate law (Equation (2)) is used for both the mineral dissolution and precipitation reactions.

3.5.1.2. Scenario 2: Alex case. The latest version of TOUGHREACT does not allow to input two $f(\Delta G_r)$ terms for mineral dissolution rate laws. Thus, we test the

Table II. Initial mineral volume fractions and possible mineral phases used in the simulations.

Minerals introduced in the model	Chemical formula	Volume percent (%)*
Quartz	SiO_2	69.95
K-feldspar	$KAlSi_3O_8$	24
Oligoclase	$Ca_{0.2}Na_{0.8}Al_{1.2}Si_{2.8}O_8$	0.5
Dolomite	$CaMg(CO_3)_2$	0.85
Illite	$K_{0.6}Mg_{0.25}Al_{1.8}(Al_{0.5}Si_{3.5}O_{10})(OH)_2$	4.7
Calcite	$CaCO_3$	
Anhydrite	$CaSO_4$	
Chlorite	$(Mg_{2.5}Fe_{2.5}Al)(AlSi_3)O_{10}(OH)_8$	
Low-albite	$NaAlSi_3O_8$	
Magnesite	$MgCO_3$	
Kaolinite	$Al_2Si_2O_5(OH)_4$	
Siderite	$FeCO_3$	
Ankerite	$CaMg_{0.3}Fe_{0.7}(CO3)_2$	
Dawsonite	$NaAlCO_3(OH)_2$	
Opal-A	SiO_2	
Alunite	$KAl_3(SO_4)_2(OH)_6$	
Na-smectite	$Na_{0.29}Mg_{0.26}Al_{1.77}Si_{3.97}O_{10}(OH)_2$	
Ca-smectite	$Ca_{0.145}Mg_{0.26}Al_{1.77}Si_{3.97}O_{10}(OH)_2$	
Clinochlore-14A	$Mg_5Al_2Si_3O_{10}(OH)_8$	

*Eliasson *et al.* [43] and Leeper [57].

Table III. Solution chemistry of the Mt. Simon formation brine after Eliasson *et al.* (1998).

Component	Concentration (mol/kg H_2O)
Ca	3.547×10^{-1}
Mg	1.033×10^{-1}
Na	1.596
K	3.108×10^{-2}
Fe	3.161×10^{-5}
C	1.724×10^{-3}
S	1.408×10^{-2}
Cl	2.545
pH	6.9
Temperature	75 °C

Alekseyev *et al.* [22] type rate law (Equation (4), called 'Alex law' hereafter) for feldspar dissolution. In order to ensure that the effects of Alex law is closer to the Burch-type law, we conduct a nonlinear fitting with an excel solver to determine the parameters of p and q in Equation (4) (Figure 1a). The curve of Burch-type law is used as a fitting target. The parameters of m_1, n, m_2, and k_1/k_2 values are all from Hellmann and Tisserand [24], and $(k_1 + k_2)$ is normalized to be 1. The fitting at 75 °C (reservoir temperature of Mt. Simon) yields a p and a q of 0.184 and 4.04, respectively. Note that in the Alex case, only feldspar dissolution rate laws (oligoclase, K-feldspar, and albite) are changed to Alex law; all others remain to be the same as the Base case (including feldspar precipitation rate law).

3.5.1.3. *Scenario 3: BCF case.*

In this scenario, BCF-type rate law (Equation (5)) is used for all secondary mineral precipitation reactions and TST rate law for all mineral dissolution reactions.

3.5.1.4. *Scenario 4: Alex + BCF case.*

In this case, Alex law is used for feldspar dissolution and BCF-type law for secondary mineral precipitation; all others remain to be the same as the Base case.

3.5.2. Kinetic parameters

To calculate the kinetic rate constant k in Equation (1), not only the neutral pH mechanism but also acid and base mechanisms should be taken into account. This is because dissolution and precipitation are often catalyzed by H^+ (acid mechanism) and OH^- (base mechanism). Therefore, a general form for k, including the three mechanisms, is as follows [49]:

$$k = k_{nu}^{25}\exp\left[\frac{-E_{nu}}{R}\left(\frac{1}{T}-\frac{1}{298.15}\right)\right] + k_H^{25}\exp\left[\frac{-E_H}{R}\left(\frac{1}{T}-\frac{1}{298.15}\right)\right]a_H^{n_H} + k_{OH}^{25}\exp\left[\frac{-E_{OH}}{R}\left(\frac{1}{T}-\frac{1}{298.15}\right)\right]a_{OH}^{n_{OH}} \quad (6)$$

where subscripts nu, H, and OH indicate neutral, acid, and base mechanisms, respectively; k^{25} is the rate constant at 25 °C; E is the apparent activation energy; R is the universal gas constant; T is the absolute temperature; a is the activity of the aqueous species; and n is a power term.

For each mineral controlled by kinetics in our simulations, the acid or base mechanism is taken into consideration for mineral dissolution reactions only. Precipitation reactions only employ a neutral pH mechanism because of the lack of precipitation rate data at different pH for most minerals. Kinetic parameters employed here are similar to those used in Xu *et al.* [44], which are listed in Table IV.

4. RESULTS

4.1. Alex case

4.1.1. Feldspar dissolution

Compared with Base case, using Alex law for feldspar dissolution does not make significant changes for rates of oligoclase dissolution patterns (diagrams not shown). The initial abundance of oligoclase is low, only 0.5%, and it

Int. J. Energy Res. 2015; **39**:1890–1908 © 2015 John Wiley & Sons, Ltd.
DOI: 10.1002/er

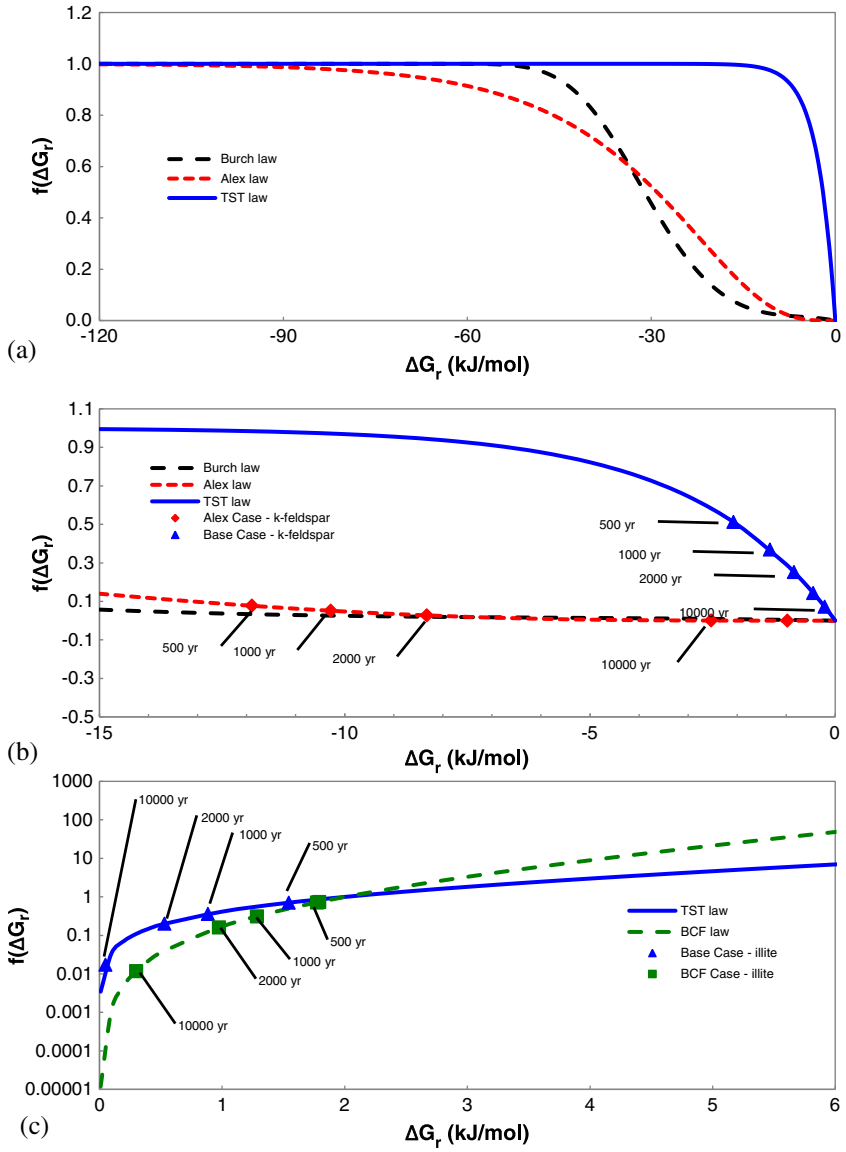

Figure 1. Relationship between f(ΔG_r) and ΔG_r for different rate laws. Scatter points are the related data of K-feldspar or illite extracted from the corresponding cases at ~2500 m from year 500 to 10,000. (a) Comparison of feldspar dissolution rate laws. The curve of TST rate law differs significantly from Burch and Alex laws in the transition and near equilibrium regions. Alex law is used to represent Burch law, as a compromise of the code capability. (b) Zoom in of (a) in the near equilibrium region with data points extracted from the simulations. (c) Comparison of illite precipitation rate laws with data points extracted from the simulations. TST, transition state theory; BCF, Burton–Cabrera–Frank.

almost completely dissolves at ~year 1000 in the acidic zones because of the influence of CO_2 injection and ~year 2000 in the zones without the effects of CO_2 in both Base and Alex cases. Oligoclase is highly undersaturated in both Base and Alex cases (SI (saturation index) < -15; $\Delta G_r < 100$ kJ/mol), and the rate law dependence on ΔG_r is small as a result (Figure 1a).

K-feldspar dissolution rates, however, decrease significantly using Alex law compared with Base case (Figure 3a, b), especially in the acidic regions caused by CO_2 injection (Figure 5a, b). The dissolution rate of K-feldspar in Base case reaches a maximum value of $\sim 2.5 \times 10^{-11}$ mol/kg H_2O/s at year 100 in the acidic region, while the maximum dissolution rate in Alex case is only 3.3×10^{-12} mol/kg H_2O/s (Figure 3a, b). The calculated $f(\Delta G_r)$ of K-feldspar in Base case is much higher than in Alex case. For example, the maximum $f(\Delta G_r)$ of K-feldspar in Base case is ~0.5 at ~2500 m, while it is only ~0.08 in Alex case (Figure 1b). Because reactive surface areas of K-feldspar in both Base case and Alex case vary only in a narrow

Table IV. Adopted kinetic data for minerals*.

Mineral	k_H (E_a) (mol/m^2/s^1) (kJ/mol)	k_{H2O} (E_a) (mol/m^2/s^1) (kJ/mol)	n	Specific surface area (cm^2/g)	Rate law (Base case)	Rate law (Alex case)	Rate law (BCF case)	Rate law (Alex + BCF case)
Quartz		1.023×10^{-14} (87.7)		9.8	TST	TST	Dissolution: TST; Precipitation BCF	Dissolution: TST; Precipitation BCF
K-feldspar	8.710×10^{-11} (51.7)	3.890×10^{-13} (38)	0.5	9.8	TST	Dissolution: Alex; Precipitation: TST	Dissolution: TST; Precipitation BCF	Dissolution: Alex; Precipitation BCF
Oligoclase	2.138×10^{-10} (65)	1.445×10^{-12} (69.8)	0.457	9.8	TST	Dissolution: Alex; Precipitation: TST	Dissolution: TST; Precipitation BCF	Dissolution: Alex; Precipitation BCF
Dolomite	6.457×10^{-4} (36.1)	2.951×10^{-8} (52.2)	0.5	9.8	TST	TST	Dissolution: TST; Precipitation BCF	Dissolution: TST; Precipitation BCF
Illite	1.047×10^{-11} (23.6)	1.660×10^{-13} (35)	0.34	151.63	TST	TST	Dissolution: TST; Precipitation BCF	Dissolution: TST; Precipitation BCF
Anhydrite					Equilibrium	Equilibrium	Equilibrium	Equilibrium
Calcite					Equilibrium	Equilibrium	Equilibrium	Equilibrium
Opal-A		Dissolution: 4.9×10^{-13} (76) Precipitation: 3.8×10^{-10} (49.8)		9.8	TST	TST	Dissolution: TST; Precipitation BCF	Dissolution: TST; Precipitation BCF
Chlorite		2.512×10^{-12} (62.76)		9.8	TST	TST	Dissolution: TST; Precipitation BCF	Dissolution: TST; Precipitation BCF
Low-albite	6.918×10^{-11} (65)	2.754×10^{-13} (69.8)	0.457	9.8	TST	Dissolution: Alex; Precipitation: TST	Dissolution: TST; Precipitation BCF	Dissolution: Alex; Precipitation BCF
Magnesite	4.619×10^{-7} (14.4)	4.517×10^{-10} (23.5)	1	9.8	TST	TST	Dissolution: TST; Precipitation BCF	Dissolution: TST; Precipitation BCF
Ankerite	6.457×10^{-4} (36.1)	1.260×10^{-9} (62.76)	0.5	9.8	TST	TST	Dissolution: TST; Precipitation BCF	Dissolution: TST; Precipitation BCF
Dawsonite	6.457×10^{-4} (36.1)	1.260×10^{-9} (62.76)	0.5	9.8	TST	TST	Dissolution: TST; Precipitation BCF	Dissolution: TST; Precipitation BCF
Siderite	6.457×10^{-4} (36.1)	1.260×10^{-9} (62.76)	0.5	9.8	TST	TST	Dissolution: TST; Precipitation BCF	Dissolution: TST; Precipitation BCF
Kaolinite	4.898×10^{-12} (65.9)	6.918×10^{-14} (22.2)	0.777	151.63	TST	TST	Dissolution: TST; Precipitation BCF	Dissolution: TST; Precipitation BCF
Alunite		1.000×10^{-12} (57.78)		9.8	TST	TST	Dissolution: TST; Precipitation BCF	Dissolution: TST; Precipitation BCF

(*Continues*)

DOI: 10.1002/er

Table IV. (Continued)

Mineral	k_H (E_a) (mol/m^2/s^1) (kJ/mol)	k_{H2O} (E_a) (mol/m^2/s^1) (kJ/mol)	n	Specific surface area (cm^2/g)	Rate law (Base case)	Rate law (Alex case)	Rate law (BCF case)	Rate law (Alex + BCF case)
Na-Smectite	1.047×10^{-11} (23.6)	1.660×10^{-13} (35)	0.34	151.63	TST	TST	Dissolution: TST; Precipitation BCF	Dissolution: TST; Precipitation BCF
Ca-Smectite	1.047×10^{-11} (23.6)	1.660×10^{-13} (35)	0.34	151.63	TST	TST	Dissolution: TST; Precipitation BCF	Dissolution: TST; Precipitation BCF
Clinochlore-14A	7.762×10^{-12} (88)	3.02×10^{-13} (88)	0.5	9.8	TST	TST	Dissolution: TST; Precipitation BCF	Dissolution: TST; Precipitation BCF

BCF, Burton–Cabrera–Frank; TST, transition state theory.
*Rate constants are at 25 °C.

range (around 3.2 ± 0.2 m^2/kg H_2O) because of its high initial abundance (24%), the rate differences of K-feldspar dissolution are mainly determined by $f(\Delta G_r)$.

The solution is unsaturated with respect to albite during the simulation, and no albite precipitation is observed. Thus, we exclude the discussion of albite precipitation in all four cases.

4.1.2. Secondary mineral precipitation

Illite and quartz are the dominant secondary aluminosilicate minerals in the simulation. The maximum changes of volume fraction for illite and quartz in Base case are ~2% and ~1%, respectively (Figure 2a), but are only ~0.5% and ~0.3%, respectively, in Alex case (Figure 2b). The maximum precipitation rate of illite drops from ~3.2×10^{-11} mol/kg H_2O/s in the acid region at year 100 in Base case to ~2.5×10^{-11} mol/kg H_2O/s in Alex case (Figure 4a, b). This dropping is approximately consistent with and likely to be mainly caused by the differences in the $f(\Delta G_r)$ of illite (the maximum $f(\Delta G_r)$ value of illite in Base case is about 1.3 times higher than that in Alex case). Similarly, the maximum quartz precipitation rate decreases from ~6×10^{-11} mol/kg H_2O/s in Base case to ~4.5×10^{-11} mol/kg H_2O/s in Alex case because less $SiO_{2(aq)}$ is released from K-feldspar dissolution in Alex case.

4.1.3. pH

A low pH zone with pH ~4.5 is observed in Base case in ~0–200 m at year 100, 1500–2500 m at year 1000, 2500–4000 m at year 5000, and disappears afterwards (being buffered to a higher pH: ~5.5 at year 10,000). In Alex case, however, the same low pH zone persists after year 5000 and migrates to 4000–6000 m at year 10,000 (Figure 5a, b).

4.1.4. Carbonate minerals and the fate of the injected CO_2

Considering the use of the same precipitation rate laws for the carbonate mineral precipitation for both Base and Alex cases, the abundance of carbonate minerals mainly reflects the neutralization capacity of feldspars on pH. Less calcite precipitation is observed in Alex case (maximum VF 0.68%) than in Base case (maximum VF 0.73%), especially in the 0–4000 radial distance. Amounts of magnesite precipitation are similar in both Alex and Base cases.

In this paper, for accounting purposes, we combined structural and residual trapping into one trapping mechanism, that is, hydrodynamic trapping. The percentage of different tapping mechanisms as a function of time is shown in Figure 6. The mineral trapping is mainly contributed by calcite and magnesite precipitation, and its percentage reduces from ~45% in Base case to only ~22% in Alex case at year 10,000 (Figure 6e).

4.2. BCF case

Compared with Base case, BCF case does not make significant changes for the patterns of feldspar dissolutions, secondary mineral precipitations, pH, and the fate of injected CO_2 (Figure 2a, c; Figure 3a, c; Figure 4a, c; Figure 5a, c; and Figure 6a, c). Generally, the mineral fraction changes are slightly smaller in BCF case than in Base case (Figure 2a, c), and the percentage of mineral trapping is slightly lower in BCF case than in Base case (Figure 6a, c). This indicates that secondary mineral precipitation rate law is not the dominant factor in determining the system behavior.

4.3. Alex + BCF case

Comparing Alex + BCF case with Alex case, the patterns of feldspar dissolutions, dominant secondary precipitations, pH, and the fate of injected CO_2 do not change significantly (Figure 2b, d; Figure 3b, d; Figure 4b, d; Figure 5b, d; Figure 6b, d). In Alex + BCF case, the maximum dissolution rate of K-feldspar is $\sim 3 \times 10^{-12}$ mol/kg H_2O/s in the acidic region; the maximum precipitation rate of illite and quartz are $\sim 2.5 \times 10^{-11}$ mol/kg H_2O/s and $\sim 4.3 \times 10^{-11}$ mol/kg H_2O/s, respectively; mineral trapping fraction at year 10,000 is ~22%. These values are almost the same as those in Alex case.

5. DISCUSSION

5.1. Coupling between K-feldspar dissolution and illite/quartz precipitation

Coupled feldspar dissolution–secondary mineral precipitation has been studied in a series of experiments [18,50–52]. This coupling is driven by common ion effects in the solution. For example, K-feldspar dissolution releases Al and Si into the solution, and the same aqueous components are consumed by kaolinite precipitation. Because the secondary kaolinite precipitation is slow, high

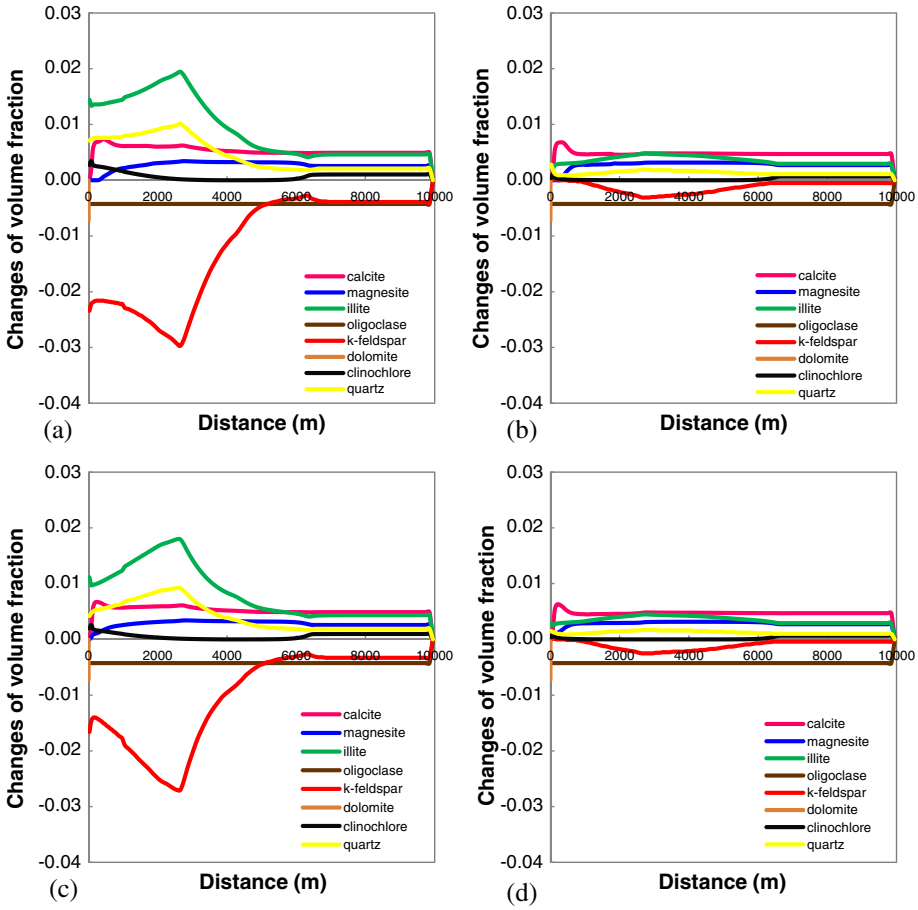

Figure 2. Comparison of simulated results of mineral volume fraction changes, as function of radial distance at year 10,000. (a) Base case with transition state theory (TST) law for both feldspar dissolution and mineral precipitation; (b) Alex case with Alex law for feldspar dissolution and TST law for mineral precipitation; (c) Burton–Cabrera–Frank (BCF) case with TST law for feldspar dissolution and BCF law for mineral precipitation; (d) Alex + BCF case with Alex law for feldspar dissolution and BCF law for mineral precipitation.

Int. J. Energy Res. 2015; **39**:1890–1908 © 2015 John Wiley & Sons, Ltd.
DOI: 10.1002/er

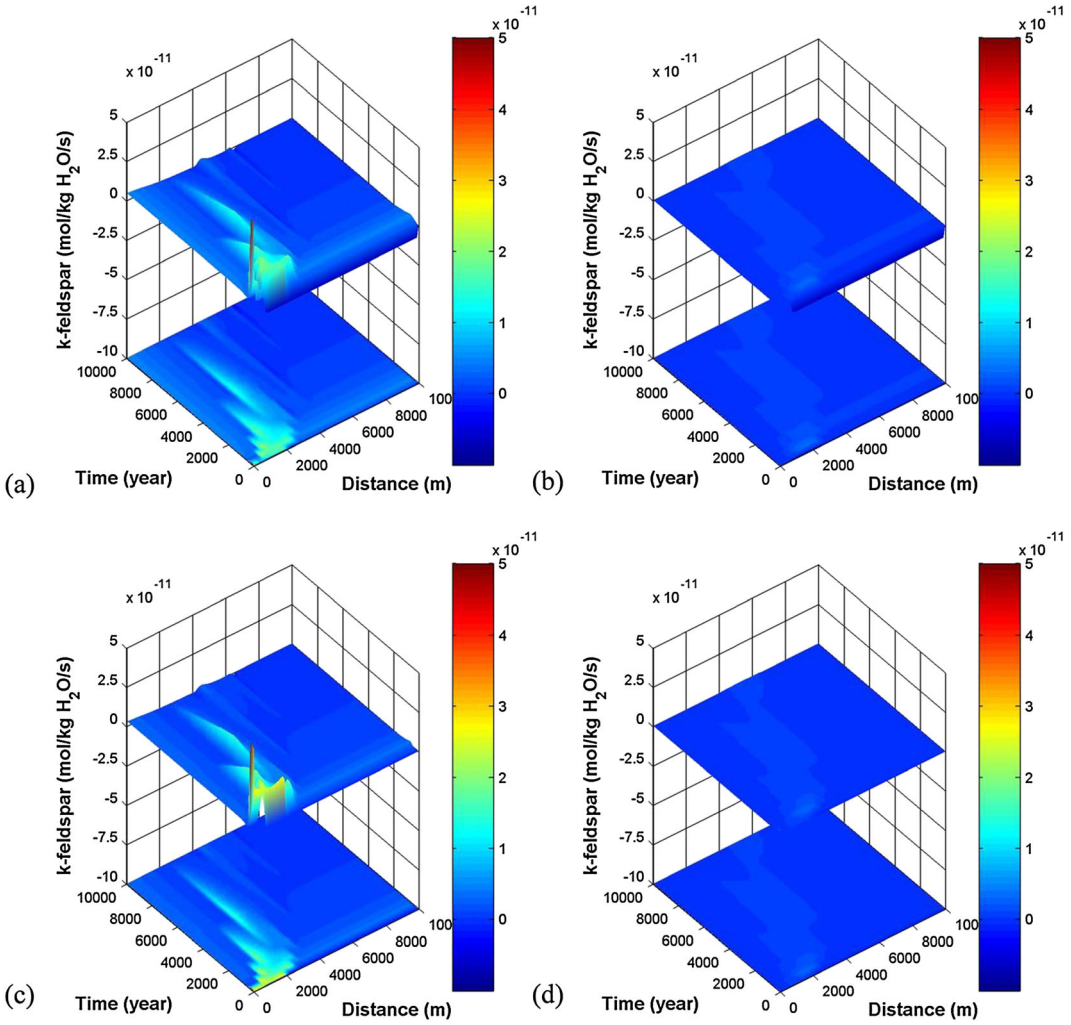

Figure 3. Reaction rates of K-feldspar (mol/kg H_2O/s) as function of radial distance and time. (a) Base case with transition state theory (TST) law for both feldspar dissolution and mineral precipitation; (b) Alex case with Alex law for feldspar dissolution and TST law for mineral precipitation; (c) Burton–Cabrera–Frank (BCF) case with TST law for feldspar dissolution and BCF law for mineral precipitation; (d) Alex + BCF case with Alex law for feldspar dissolution and BCF law for mineral precipitation.

concentrations of Al and Si are accumulated into the solution because of fast K-feldspar dissolution. This accumulation inhibits K-feldspar dissolution and promotes kaolinite precipitation by raising their saturation states. Eventually, the releasing and consuming rates of Al and Si approach the balance and rate ratios of K-feldspar dissolution versus kaolinite precipitation approaches the stoichiometric ratio of the overall reaction. The system thus reaches a steady state, and K-feldspar dissolution and kaolinite precipitation are coupled.

Because K-feldspar and illite are the most abundant primary and secondary aluminosilicate minerals, respectively, the coupling reaction between K-feldspar and illite is the dominant reaction during the simulation time (Figure 2a, Equation (7)). Concurrent dissolution of K-feldspar and illitization play the primary role in the generation of illite [53]. The intimate association of illite with K-feldspar is often observed in nature [54]. The overall reaction of K-feldspar dissolution and illite/quartz precipitation can be written as follows:

$$2.3\ \text{K-feldspar} + 0.25\ \text{Mg}^{+2}\ 1.2\ \text{H}^{+} + 0.4\text{H}_2\text{O} = \text{Illite} + 3.4\ \text{Quartz} + 1.7\ \text{K}^{+} \quad (7)$$

Dissolution of K-feldspar will consume H^+ and release Al and Si and thus alter the saturation states of illite and quartz. Proton consumption will affect the carbonate speciation and precipitation of carbonate minerals (Equations (8) and (9)):

$$\text{CO}_{2(\text{g})} + \text{H}_2\text{O} = \text{CO}_{2(\text{aq})} + \text{H}_2\text{O} = \text{HCO}_3\text{-} + \text{H}^{+} \quad (8)$$

$$\text{Mg}^{+2} + \text{HCO}_3\text{-} = \text{Magnesite} + \text{H}^{+};\ \text{Ca}^{+2} + \text{HCO}_3\text{-} = \text{Calcite} + \text{H}^{+} \quad (9)$$

Hence, the coupling between K-feldspar and illite dominates long-term mineral trapping. Note, the stoichiometric

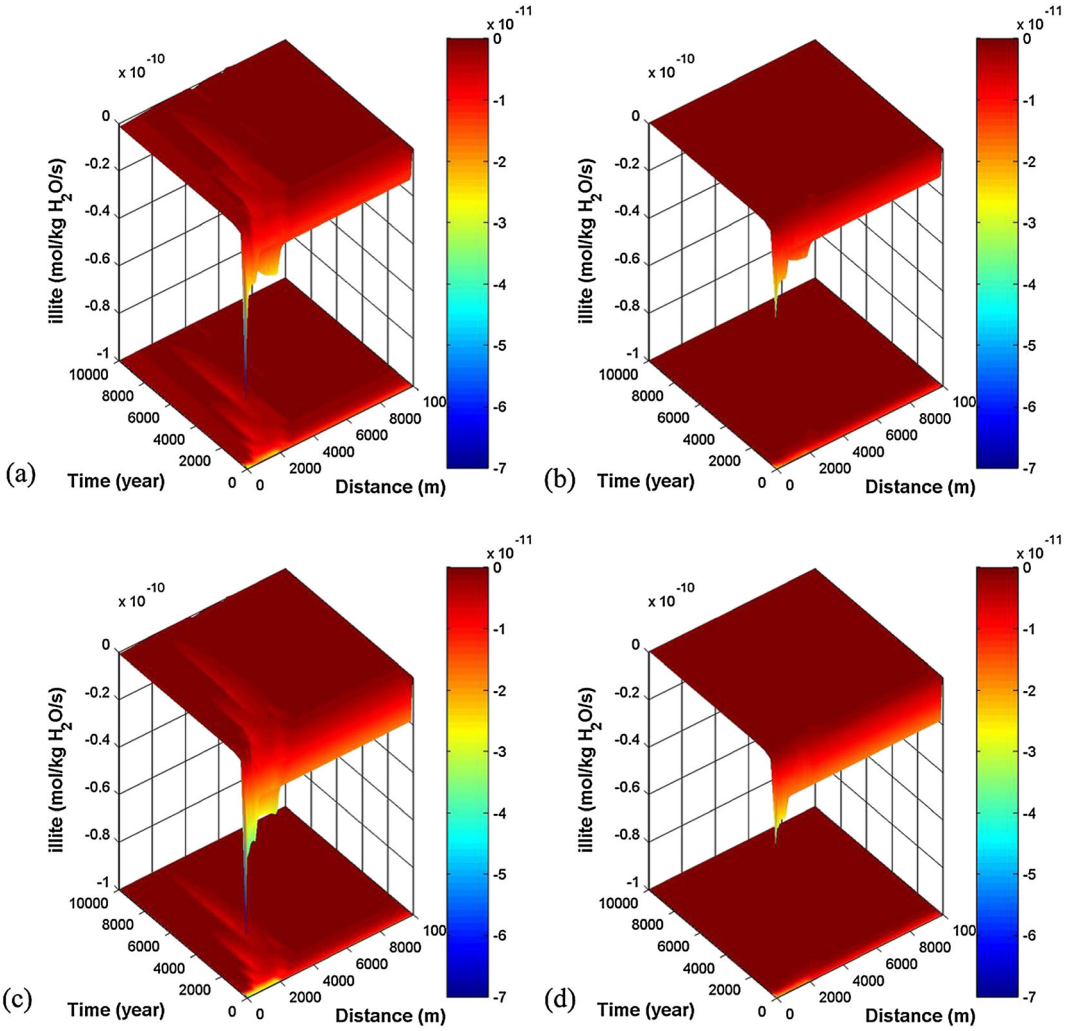

Figure 4. Reaction rate of illite (mol/kg H_2O/s), as function of radial distance and time. (a) Base case with transition state theory (TST) law for both feldspar dissolution and mineral precipitation; (b) Alex case with Alex law for feldspar dissolution and TST law for mineral precipitation; (c) Burton–Cabrera–Frank (BCF) case with TST law for feldspar dissolution and BCF law for mineral precipitation; (d) Alex + BCF case with Alex law for feldspar dissolution and BCF law for mineral precipitation.

ratio of K-feldspar to illite is 2.3 and K-feldspar to quartz is 0.67. We will discuss in the succeeding text how rate laws affect the evolution of the coupling and safety of CO_2 sequestration.

5.1.1. Evolution of the coupling

Figure 7 shows that the coupling of K-feldspar with illite/quartz can be divided into two stages: loose and tight coupling stages. In the first stage (loose coupling), the coupling of K-feldspar with illite/quartz has not been established, and the reaction rate ratios K-feldspar dissolution versus illite/quartz precipitation are far from the corresponding stoichiometry in the overall reaction (Equation (7)). Figure 7 shows that the loose coupling stage exists for ~1000 years in Base case and in BCF case, and for ~2000 years in Alex and Alex + BCF cases. Oligoclase dissolution is an important factor causing the rate ratios to be deviated from stoichiometry, because its dissolution supplies extra Al and Si, which inhibits K-feldspar dissolution and promotes illite/quartz precipitation. Therefore, in this stage, the reaction system tends to approach a steady state where illite stoichiometric precipitation rates are roughly equal to the sum of stoichiometric rates of K-feldspar and oligoclase dissolution. Note that the coupled reaction ratios of K-feldspar/illite are closer to −2.3 in low pH zones at year 1000 (Figure 8) because oligoclase dissolution is accelerated in low pH environment and oligoclase is almost exhausted at this time. The system is thus dominantly controlled by the coupling of K-feldspar with illite/quartz.

In the 'tight coupling stage', the reaction rate ratio approximately stabilizes at the corresponding stoichiometry ratio in the overall reaction (Equation (7)), and the system reaches a second steady state. The overall

Int. J. Energy Res. 2015; **39**:1890–1908 © 2015 John Wiley & Sons, Ltd.
DOI: 10.1002/er

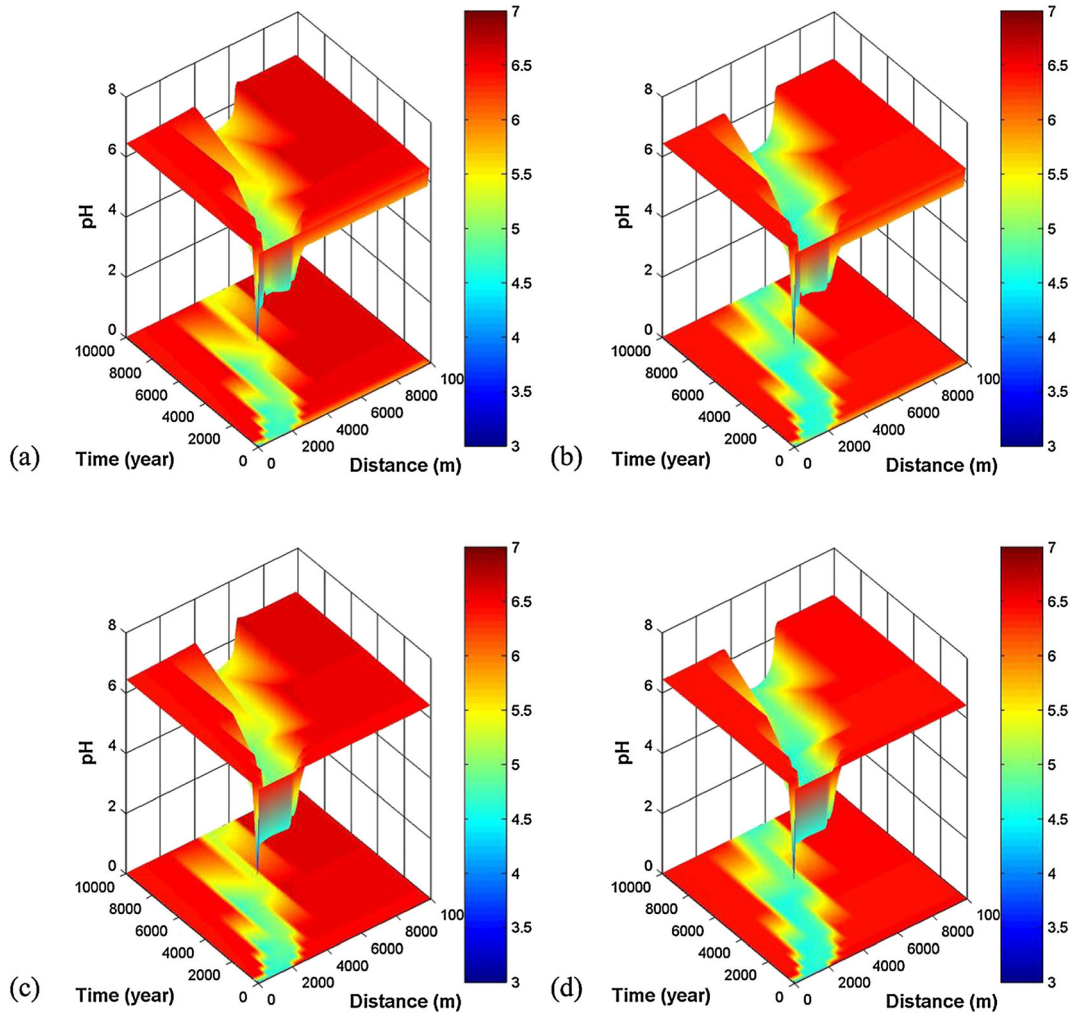

Figure 5. The pH as function of radial distance and time. (a) Base case with transition state theory (TST) law for both feldspar dissolution and mineral precipitation; (b) Alex case with Alex law for feldspar dissolution and TST law for mineral precipitation; (c) Burton–Cabrera–Frank (BCF) case with TST law for feldspar dissolution and BCF law for mineral precipitation; (d) Alex + BCF case with Alex law for feldspar dissolution and BCF law for mineral precipitation.

reaction rates decrease slowly within a long time because of the mitigation effects of illite/quartz precipitation. For example, rates of K-feldspar dissolution drops from ~2.2×10^{-13} mol/kg H_2O/s at year 2000 to ~5.4×10^{-14} mol/kg H_2O/s at year 10,000 in the zones free of CO_2 influences in Alex case. Tight coupling stage sustains for a much longer time; K-feldspar, illite/quartz reactions, and mineral trapping primarily occur at this stage (Figure 6). K-feldspar dissolution is faster than it should be at the stoichiometric ratio of K-feldspar/illite in normal pH zones (~6.5), but K-feldspar/illite ratio is closer to −2.3 in the acidic zones (Figure 8). This is because Clinochlore-14A precipitation consumes Mg, Al, and Si and promotes extra K-feldspar dissolution in the normal pH zones, but in the acidic zones, clinochlore-14A does not precipitate (Figure 9).

5.1.2. Effect of rate law on the coupling and CO_2 sequestration safety

Because calcite is assumed to be at local equilibrium and the rate constant of magnesite is several orders of magnitude larger than K-feldspar, illite, and quartz (Table IV), change of rate law for secondary mineral precipitation does not make significant changes for the patterns of K-feldspar/illite rate ratios, pH, and mineral trapping (Figures 5–8). Therefore, we focus on comparing Alex case with Base case.

The H^+ consumption is much less in Alex case than in Base case (Equation (7)) because Alex law decreases the maximum K-feldspar dissolution rate and thus the overall reaction rates of K-feldspar and illite/quartz. Solution pH, therefore, rises more quickly in Base case than in Alex case. Larger amount of carbon is trapped into the mineral phase in Base case than in Alex case (Figure 6) as higher

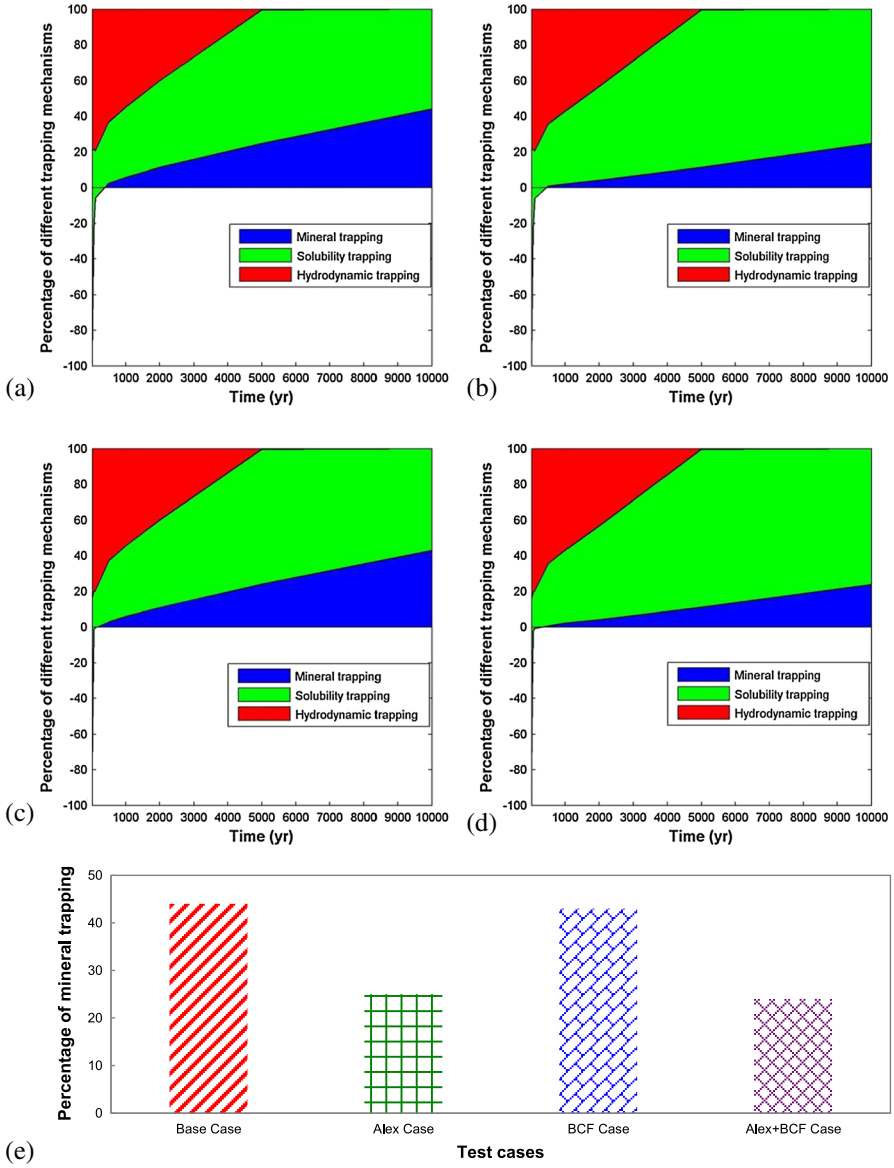

Figure 6. Percentage of different trapping mechanisms for the whole domain as function of time. (a) Base case with transition state theory (TST) law for both feldspar dissolution and mineral precipitation; (b) Alex case with Alex law for feldspar dissolution and TST law for mineral precipitation; (c) Burton–Cabrera–Frank (BCF) case with TST law for feldspar dissolution and BCF law for mineral precipitation; (d) Alex + BCF case with Alex law for feldspar dissolution and BCF law for mineral precipitation. (e) Percentage of total injected CO_2 as mineral trapping after 10,000 years for the whole domain.

pH promotes faster precipitation of calcite and magnesite (Equation (9)). These indicate that using TST rate law for feldspar dissolution may overestimate mineral trapping.

5.2. Comparison with previous work

Zhu *et al.* [19] simulated the feldspar hydrolysis experiments with reaction path model to explore how feldspar dissolution and secondary precipitations are coupled in batch reactor experimental systems. One set of experiment data is from Alekseyev *et al.* [22], who conducted batch experiments for albite dissolution in 0.1 m $KHCO_3$ fluid at 300 °C, 88 bars, and pH ~9.0 (buffered by bicarbonate). The measured initial Brunauer–Emmett–Teller specific surface areas were 0.12 m^2/g for albite, and X-ray diffraction and scanning electron microscopy results show that sanidine was the only secondary mineral. Zhu *et al.* [19] found that (1) the preliminary stage (loose coupling) before tight coupling between albite and sanidine is relatively shorter (<672 h) when compared with the time needed for the complete dissolution of albite (3650 h). The tight coupling stage will be even longer if more albite is present;

Int. J. Energy Res. 2015; **39**:1890–1908 © 2015 John Wiley & Sons, Ltd.
DOI: 10.1002/er

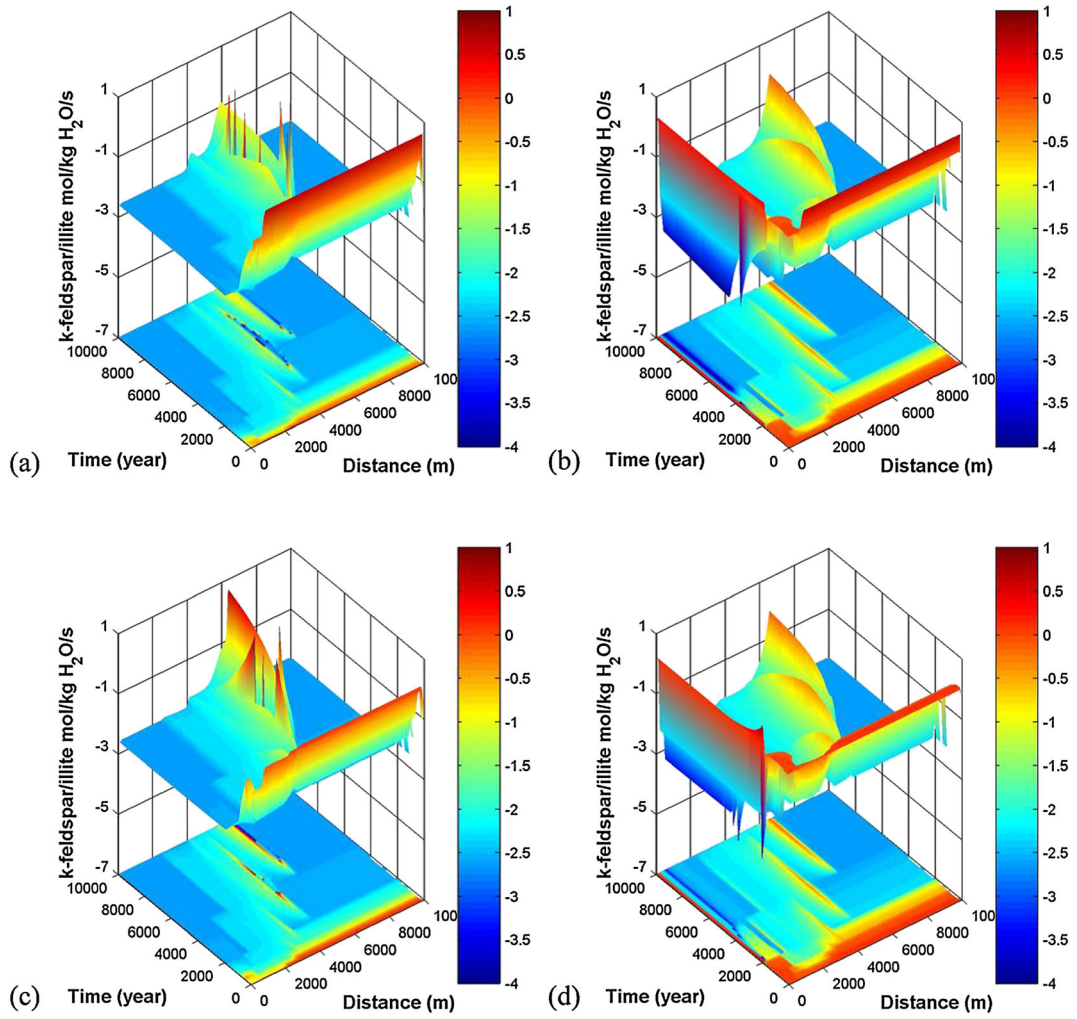

Figure 7. Reaction rate ratios between K-feldspar and illite as function of radial distance and time. (a) Base case with transition state theory (TST) law for both feldspar dissolution and mineral precipitation; (b) Alex case with Alex law for feldspar dissolution and TST law for mineral precipitation; (c) Burton–Cabrera–Frank (BCF) case with TST law for feldspar dissolution and BCF law for mineral precipitation; (d) Alex + BCF case with Alex law for feldspar dissolution and BCF law for mineral precipitation.

(2) with the sigmoidal shape rate law for primary mineral dissolution (the Burch-type law), the influence of the ΔG_r term takes effect earlier, and the rates drop faster than TST rate law in the course of approaching equilibrium; (3) The precipitation of the secondary minerals is the liming step that controls the dissolution rate of the primary mineral.

Although the system (minerals, aqueous solution, and CO_2) is much more complex in our current simulation work than that in Zhu *et al.* [19] and it is a flow instead of a static system, the conclusions drawn from Zhu *et al.* [19] remain valid. We find that (1) the loose coupling stage is much shorter than the tight coupling stage; (2) the influence of the ΔG_r term for K-feldspar takes effect at a lower ΔG_r value away from the equilibrium, if using Alex law for feldspar dissolution instead of TST law; (3) illite/quartz precipitation is the rate controller for the overall reaction.

The major differences between the two studies are (1) the coupling of K-feldspar dissolution and illite/quartz is disturbed because of oligoclase dissolution and Clinochlore-14A precipitation; (2) ΔG_r for K-feldspar increases from –8.3 kJ/mol at year 2000 to –2.5 kJ/mol at year 10,000 (Figure 1b), rather than locked at a fixed value, as in Zhu *et al.* [19].

Pham *et al.* [55] investigated how the rate model (BCF + CNT model; CNT (classical nucleation theory)) that takes into account both nucleation and growth of secondary mineral phases influences CO_2 portion trapped in mineral in a batch system for Utsira-type reservoirs. Their results suggest that using TST instead of BCF + CNT law for mineral precipitation largely overestimated the growth potential of carbonates such as dawsonite, magnesite, and dolomite. In contrast, our simulation shows that using TST instead of BCF

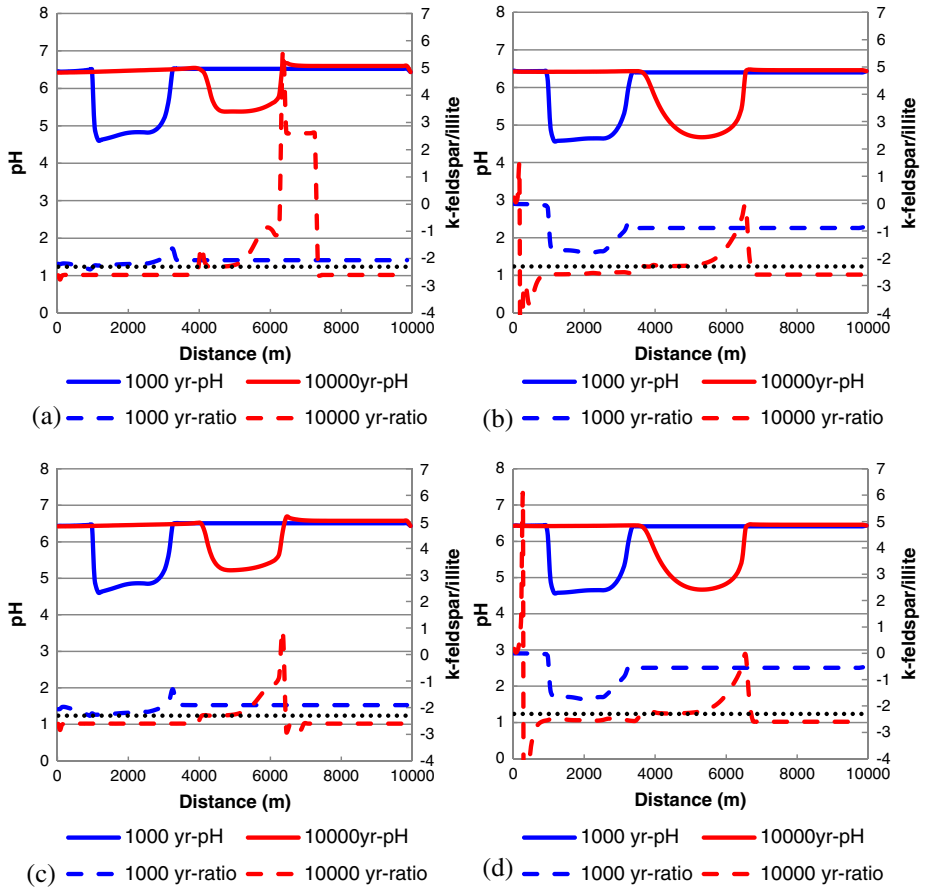

Figure 8. Comparison of pH and the reaction rate ratios of K-feldspar versus illite, as function of radial distance at year 1000 and 10,000. (a) Base case with transition state theory (TST) law for both feldspar dissolution and mineral precipitation; (b) Alex case with Alex law for feldspar dissolution and TST law for mineral precipitation; (c) Burton–Cabrera–Frank (BCF) case with TST law for feldspar dissolution and BCF law for mineral precipitation; (d) Alex + BCF case with Alex law for feldspar dissolution and BCF law for mineral precipitation. The black dotted lines represent the stoichiometric ratio of K-feldspar/illite in the overall reaction (2.3).

precipitation law does not make significant changes for the percentage of mineral trapping. The main reason for this discrepancy is that BCF + CNT law considers nucleation processes, and secondary minerals need to overcome a certain threshold SI in order to precipitate, which significantly influences the paragenetic sequence and results in a large difference in mineral trapping.

Balashov *et al.* [8] investigated the fate of injected CO_2 with a reactive diffusion model that was solved by program MK76. They observed coupling among primary and secondary minerals when analyzing the impact of kinetic rate constants on stored CO_2. For example, when the rate constant of oligoclase increases, the maximum volume fractions of both smectite and albite rise correspondently. However, they did not investigate further how the minerals interact with each other, the mathematics and chemistry behind the coupling, and how the coupling affects the fate of injected CO_2. In this paper, we studied the mechanism of coupled reactions and how the coupling evolves and discovered that the coupling of K-feldspar with illite/quartz is the dominant process controlling the long-term mineral trapping.

To date, only a few studies have focused on the effect of rate laws on CO_2 trapping in the deep saline aquifer. In this paper, we investigated a sandstone formation resembling the Mt. Simon saline aquifer in the Midwest, USA, which has abundant feldspar. However, systems with different initial sandstone compositions, water chemistry, and reservoir conditions may have different types of mineral coupling, and the role of rate laws may also vary case by case. The rate laws considered here are only TST, Alex, and BCF laws. Pham *et al.* [55] suggested the nucleation process significantly influences the paragenetic sequence of secondary mineralization, resulting in a larger difference in mineral trapping. Additionally, Burch-type law [23] is better to delineate the evolution of feldspar dissolution rates near equilibrium. Therefore, further work is still needed to explore

Int. J. Energy Res. 2015; **39**:1890–1908 © 2015 John Wiley & Sons, Ltd.
DOI: 10.1002/er

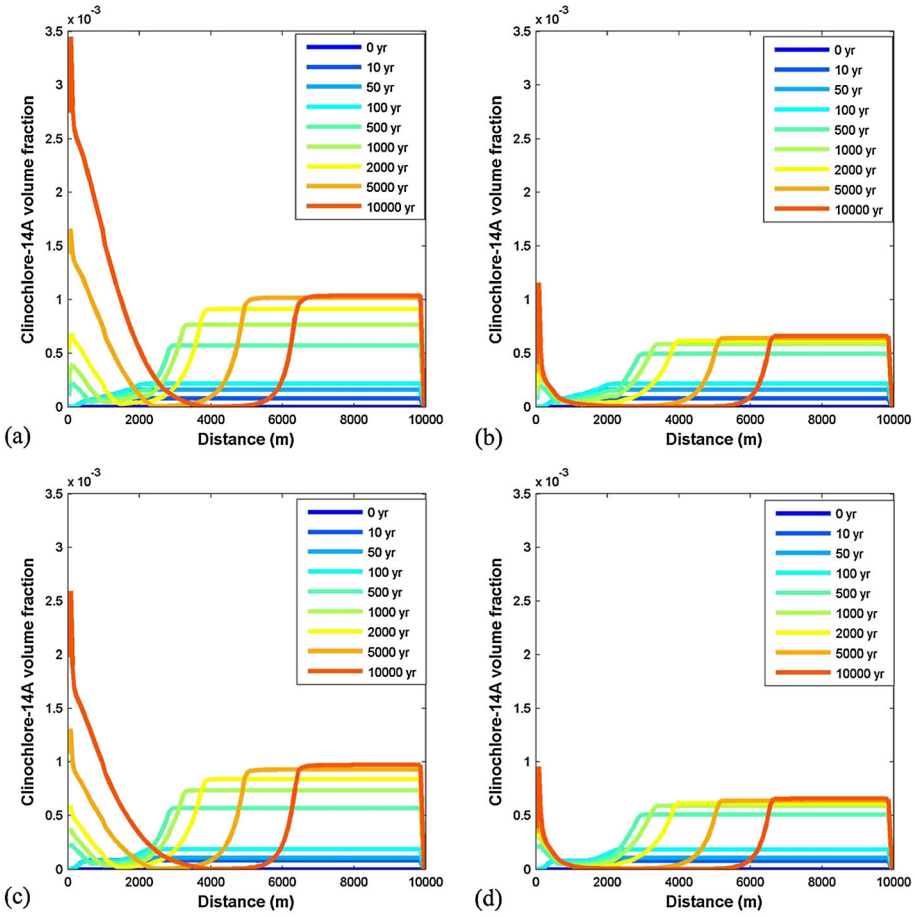

Figure 9. Clinochlore-14A volume fraction as function of radial distance and time. (a) Base case with transition state theory (TST) law for both feldspar dissolution and mineral precipitation; (b) Alex case with Alex law for feldspar dissolution and TST law for mineral precipitation; (c) Burton–Cabrera–Frank (BCF) case with TST law for feldspar dissolution and BCF law for mineral precipitation; (d) Alex + BCF case with Alex law for feldspar dissolution and BCF law for mineral precipitation.

how the factors listed previously affect the effect of rate law on CO_2 sequestration.

6. CONCLUSIONS AND REMARKS

We conducted a reactive transport model for CO_2 sequestration in a sandstone formation resembling the Mt. Simon saline reservoir. Four rate law scenarios were constructed to investigate whether rate law uncertainties have large effect on CO_2 sequestration, how these effects work, and what role the coupling between feldspar dissolution and secondary mineral precipitation plays in the effect. Our conclusions are presented as follows:

1. The coupled K-feldspar dissolution with illite/quartz precipitation is the dominant reaction because of the high initial K-feldspar abundance (24%) and illite/quartz to be the most abundant secondary aluminosilicate minerals. Therefore, H^+ consumption is primarily dominated by this coupling, which increases pH and HCO_3^- concentration in the solution, and promotes precipitation of carbonate minerals.
2. Mineral trapping is more sensitive to the rate laws on feldspar dissolution than to rate laws on carbonate mineral precipitation. This is because carbonate mineral precipitation rates are fast compared with feldspar dissolution and silicate secondary mineral precipitation. In the network of reactions, the slowest reactions dominate the whole process.
3. Negligence of the sigmoidal shape of rate – ΔG_r relationships and the mitigating effects secondary mineral precipitation can overestimate both the extent of feldspar dissolution during CO_2 injection and the extent of mineral trapping.

Our present work focuses on the Mt. Simon sandstone-type reservoir and a limited number of rate laws (TST, BCF, and Alex laws). Further work is still needed to explore how initial sandstone compositions, water chemistry, and reservoir conditions affect the effect of rate law on CO_2 sequestration.

ACKNOWLEDGEMENTS

We acknowledge the support of the US Department of Energy grant DE-FE0004381 and U.S. NSF grant EAR-1225733. Although the work was partly sponsored by an agency of the United States Government, the views and opinions of authors expressed herein do not necessarily state or reflect those of the United States Government or any agency thereof. We thank Sean Miranda for the editorial assistance. Financial support from China Scholarship Council for G. R. Z. is also gratefully acknowledged.

REFERENCES

1. Desideri U, Arcioni L, Tozzi M. Feasibility study for a carbon capture and storage project in northern Italy. *International Journal of Energy Research* 2008; **32**:1175–1183.
2. Holloway S. Underground sequestration of carbon dioxide – a viable greenhouse gas mitigation option. *Energy* 2004; **30**:2318–2333.
3. Soong Y, Hedges SW, Howard BH, Dilmore RM, Allen DE. Effect of contaminants from flue gas on CO_2 sequestration in saline formation. *International Journal of Energy Research* 2014; **38**:1224–1232.
4. Ji X, Zhu C. CO_2 storage in deep saline aquifers. *Chapter 10 in Novel Materials for Carbon Dioxide Mitigation Technology*. Elsevier, 2015; 299–332. http://dx.doi.org/10.1016/B978-0-444-63259-3.00010-0.
5. Bachu S, Bonijoly D, Bradshaw J, Burruss R, Holloway S, Christensen NP, Mathiassen OM. CO_2 storage capacity estimation: methodology and gaps. *International Journal of Greenhouse Gas Control* 2007; **1**:430–443.
6. Gunter WD, Bachu S, Benson S. The role of hydrogeological and geochemical trapping in sedimentary basins for secure geological storage of carbon dioxide. *Geological Society, London, Special Publications* 2004; **233**:129–145.
7. IPCC. Special report on carbon dioxide capture and storage. Intergovernmental Panel on Climate Change, 2005.
8. Balashov VN, Guthrie GD, Hakala JA, Lopano CL, Rimstidt JD, Brantley SL. Predictive modeling of CO_2 sequestration in deep saline sandstone reservoirs: impacts of geochemical kinetics. *Applied Geochemistry* 2013; **30**:41–56.
9. Gaus I, Azaroual M, Czernichowski-Lauriol I. Reactive transport modelling of the impact of CO_2 injection on the clayey cap rock at Sleipner (North Sea). *Chemical Geology* 2005; **217**:319–337.
10. Liu F, Lu P, Zhu C, Xiao Y. Coupled reactive flow and transport modeling of CO_2 sequestration in the Mt. Simon sandstone formation, Midwest U.S.A. *International Journal of Greenhouse Gas Control* 2011; **5**:294–307.
11. Mohd Amin S, Weiss DJ, Blunt MJ. Reactive transport modelling of geologic CO_2 sequestration in saline aquifers: the influence of pure CO_2 and of mixtures of CO_2 with CH_4 on the sealing capacity of cap rock at 37 degrees C and 100 bar. *Chemical Geology* 2014; **367**:39–50.
12. Johnson JW, Nitao JJ, Knauss KG. Reactive transport modelling of CO_2 storage in saline aquifers to elucidate fundamental processes, trapping mechanisms and sequestration partitioning. *Geological Society, London, Special Publications* 2004; **233**:107–128.
13. Audigane P, Gaus I, Czernichowski-Lauriol I, Pruess K, Xu T. Two-dimensional reactive transport modeling of CO_2 injection in a saline aquifer at the Sleipner site, North Sea. *American Journal of Science* 2007; **307**:974–1008.
14. Blum A, Stillings L. Feldspar dissolution kinetics. In *Chemical Weathering Rates of Silicate Minerals*, Brantley SL, White AR (eds.). Mineralogical Society of America: Washington DC, 1995; 291–346.
15. Zhu C. Geochemical modeling of reaction paths and geochemical reaction networks. In *Thermodynamics and Kinetics of Water–rock Interaction*, Oelkers EH, Schott J (eds.). Mineralogical Society of America: Washington, 2009; 533–569.
16. Zhu C, Blum AE, Veblen DRD. A new hypothesis for the slow feldspar dissolution in groundwater aquifers. *Geochimica et Cosmochimica Acta* 2004; **68**:A148.
17. Maher K, Steefel CI, White AF, Stonestrom DA. The role of reaction affinity and secondary minerals in regulating chemical weathering rates at the Santa Cruz Soil Chronosequence, California. *Geochimica et Cosmochimica Acta* 2009; **73**(10):2804–2831.
18. Zhu C, Lu P. Coupled alkali feldspar dissolution and secondary mineral precipitation in batch systems: 3. Saturation indices of product minerals and reaction paths. *Geochimica et Cosmochimica Acta* 2009; **73**:3171–3200.
19. Zhu C, Lu P, Zheng Z, Ganor J. Coupled alkali feldspar dissolution and secondary mineral precipitation in batch systems: 4. Numerical modeling of reaction path and reactive transport. *Geochimica et Cosmochimica Acta* 2010; **74**(14):3963–3983.
20. Lu P, Fu Q, Seyfried WE, Hedges SW, Soong Y, Jones K, Zhu C. Coupled alkali feldspar dissolution and secondary mineral precipitation in batch systems-2: New experiments with supercritical CO2 and implications for carbon sequestration. *Applied Geochemistry* 2013; **30**:75–90.

21. Zhu C. Current Status of Geochemical Modeling in Environmental and Geological Studies. In *Encyclopedia of Sustainability Science and Technology*, Robert A, Meyers A (eds.). Springer: Hardcover, 2013; ISBN 978-0-387-89469-0. DOI: 10.1007/978-1-4419-0851-3.
22. Alekseyev VA, Medvedeva LS, Prisyagina NI, Meshalkin SS, Balabin AI. Change in the dissolution rates of alkali feldspars as a result of secondary mineral precipitation and approach to equilibrium. *Geochimica et Cosmochimica Acta* 1997; **61**:1125–1142.
23. Burch TE, Nagy KL, Lasaga AC. Free energy dependence of albite dissolution kinetics at 80 °C and pH 8.8. *Chemical Geology* 1993; **105**:137–162.
24. Hellmann R, Tisserand D. Dissolution kinetics as a function of the Gibbs free energy of reaction: an experimental study based on albite feldspar. *Geochimica et Cosmochimica Acta* 2006; **70**:364–383.
25. Burton WK, Cabrera N, Frank FC. The growth of crystals and the equilibrium structure of their surfaces. *Royal Society of London Philosophical Transactions* 1951; **243**:299–358.
26. Saldi GD, Jordan G, Schott J, Oelkers EH. Magnesite growth rates as a function of temperature and saturation state. *Geochimica et Cosmochimica Acta* 2009; **73**:5646–5657.
27. Leetaru H, Morse DG, Frailey SM, Finley R. Mt. Simon sandstone as a carbon sequestration sink in the Illinois Basin. AAPG Annual Convention, Calgary, Alberta, 2005.
28. Becker LE, Hreha AJ, Dawson TA. Pre-Knox (Cambrian) stratigraphy in Indiana. State of Indiana, Department of Natural Resources, Geological Survey, 1978.
29. Cohee GV. Cambrian and Ordovician rocks in Michigan Basin and adjoining areas. *AAPG Bulletin* 1948; **32**:1417–1448.
30. Bowersox JR, Williams DA, Greb S, Nuttall BC, Parris TM, Anderson WA. Solving the carbon storage puzzle in Kentucky, North-Central Section-42nd Annual Meeting, Evansville, Indiana, 2008.
31. Walcott CD. Cambrian geology and paleotology. *Smithsonian Miscellaneous Collections* 1914; **57**:345–412.
32. Yawar Z, Schieber J. Facies and depositional setting of Eau Claire Formation (Cambrian) mudstones in northwestern Indiana, Geological Society of America Abstracts with Programs, p. 435, 2008.
33. MGSC. 2011. http://sequestration.org/mgscprojects/deepsalinestorage.html.
34. ZERO. 2013. http://www.zeroco2.no/projects/mt.-simon-sandstone.
35. Kumar A, Noh M, Pope GA, Sepehrnoori K, Bryant S, Lake LW. Reservoir simulation of CO_2 storage in deep saline aquifers, 2004 SPE/DOE Symposium on Improved Oil Recovery, Tulsa, Oklahoma, 2004.
36. Leonenko Y, Keith D, Pooladi-Darvish M, Hassanzadeh Y. Accelerating the dissolution of CO_2 in aquifers, Eighth International Conference on Greenhouse Gas Control Technologies, Trondheim, Norway, 2006.
37. Spycher N, Pruess K. CO_2–H_2O mixtures in the geological sequestration of CO_2 center dot. II. Partitioning in chloride brines at 12-100 degrees C and up to 600 bar. *Geochimica et Cosmochimica Acta* 2005; **69**:3309–3320.
38. Xu T, Sonnenthal E, Spycher N, Pruess K. TOUGHREACT user's guide: a simulation program for non-isothermal multiphase reactive geochemical transport in variably saturated geologic media (V1.2), V1.2 ed. Lawrence Berkeley National Laboratory, 2004.
39. Lasaga AC, Soler JM, Ganor J, Burch TE, Nagy KL. Chemical weathering rate laws and global geochemical cycles. *Geochimica et Cosmochimica Acta* 1994; **58**:2361–2386.
40. Pruess K. ECO2N: A TOUGH2 fluid property module for mixtures of water, NaCl, and CO2. Earth Sciences Division, Lawrence Berkeley National Laboratory, 2005.
41. André L, Azaroual M, Menjoz A. Numerical simulations of the thermal impact of supercritical CO_2 injection on chemical reactivity in a carbonate saline reservoir. *Transport in Porous Media* 2010; **82**:247–274.
42. Pruess K, Olderburg C, Moridis G. TOUGH2 user's guide, version 2.0. Lawrence Berkeley National Laboratory Paper LBNL-43134, 2012.
43. Eliasson B, Riemer P, Wokaun A. *Greenhouse Gas Control Technologies: Proceedings of the 4th International Conference on Greenhouse Gas Control Technologies*. Elsevier: Amsterdam, 1998.
44. Xu T, Apps JA, Pruess K, Yamamoto H. Numerical modeling of injection and mineral trapping of CO_2 with H_2S and SO_2 in a sandstone formation. *Chemical Geology* 2007; **242**:319–346.
45. Lasaga AC. *Kinetic Theory in the Earth Sciences*. Princeton University Press: New York, 1998.
46. Lasaga AC. Rate laws of chemical reactions. In *Kinetics of Geochemical Processes*, Lasaga AC, Kirkpatrick RJ (eds.). Mineralogical Society of America: Washington DC, 1981a; 1–68.
47. Lasaga AC. Transition state theory. In *Kinetics of Geochemical Processes*, Lasaga AC, Kirkpatrick RJ (eds.). Mineralogical Society of America: Washington DC, 1981b; 135–169.
48. Hellevang H, Declercq J, Aagaard P. Why is dawsonite absent in CO_2 charged reservoirs? *Oil & Gas Science and Technology–Revue de l'IFP* 2011; **66**:119–135.

49. Palandri JL, Kharaka YK. A compilation of rate parameters of water–mineral interaction kinetics for application to geochemical modeling. *U.S. Geological Survey* 2004.
50. Lu P, Konishi H, Oelkers E, Zhu C. Coupled alkali feldspar dissolution and secondary mineral precipitation in batch systems: 5. Results of K-feldspar hydrolysis experiments. *Chinese Journal of Geochemistry* 2015; **34**:1–12.
51. Yang C, Trevino RH, Zhang T, Romanak KD, Wallace K, Lu J, Mickler PJ, Hovorka SD. Regional assessment of CO_2-solubility trapping potential: a case study of the coastal and offshore Texas Miocene interval. *Environment Science and Technology* 2014; **48**:8275–8282.
52. Zhu C, Lu P. The coupling of dissolution and precipitation reactions as the main contributor to the apparent field-lab rate discrepancy. *Procedia Earth and Planetary Science* 2013; **7**:948–952.
53. Thyne G, Boudreau BP, Ramm M, Midtbø RE. Simulation of potassium feldspar dissolution and illitization in the Statfjord Formation, North Sea. *AAPG Bulletin* 2001; **85**:621–635.
54. Meunier A, Velde BD. *Illite: Origins, Evolution, and Metamorphism*. Springer: Berlin, 2004.
55. Pham VTH, Lu P, Aagaard P, Zhu C, Hellevang H. On the potential of CO_2–water–rock interactions for CO_2 storage using a modified kinetic model. *International Journal of Greenhouse Gas Control* 2011; **5**:1002–1015.
56. Hovorka SD, Romero ML, Warne AG, Ambrose WA, Tremblay TA, Treviño RH, Sasson D. *Sequestration of Greenhouse Gases in Brine Formations*. Bureau of Economic Geology: The University of Texas at Austin, 2012.
57. Leeper N. Characterization of the Mt. Simon sandstone in southwest Ohio for CO_2 sequestration. The Ohio State University, 2012.
58. Van Genuchten MT. A closed-form equation for predicting the hydraulic conductivity of unsaturated soils. *Soil Science Society of America Journal* 1980; **44**:892–898.
59. Krevor SCM, Pini R, Zuo L, Benson SM. Relative permeability and trapping of CO_2 and water in sandstone rocks at reservoir conditions. *Water Resources Research* 2012; **48**(2): DOI: 10.1029/2011WR010859.
60. Corey AT. The interrelation between gas and oil relative permeabilities. *Producers Monthly* 1954; **19**(1):38–41.